Magnetic Resonance Imaging 63 (2019) 105–113

Contents lists available at ScienceDirect

Magnetic Resonance Imaging

journal homepage: www.elsevier.com/locate/mri

Original contribution

The utility of APT and IVIM in the diagnosis and differentiation of squamous cell carcinoma of the cervix: A pilot study

Beibei Li[a], Hongzan Sun[a,*], Siyu Zhang[a], Xiaoqi Wang[b], Qiyong Guo[a]

[a] Department of Radiology, Shengjing Hospital of China Medical University, Shenyang 110004, PR China
[b] Philips Healthcare, 7F, Tower No. 2, The World Profit Centre, No.16 Tianze Road, Chaoyang District, Beijing 100600, PR China

ARTICLE INFO

Keywords:
Magnetic resonance imaging
Amide proton transfer imaging
Intravoxel incoherent motion imaging
Uterine cervical neoplasms

ABSTRACT

Purpose: This study aimed to investigate whether amide proton transfer (APT) imaging, compared with intravoxel incoherent motion (IVIM) imaging-derived parameters, can differentiate squamous cell carcinoma of the cervix (SCCC) from the normal cervical stroma and distinguish poorly differentiated SCCC from well-moderately differentiated SCCC.

Methods: This prospective study enrolled 32 patients, comprising 20 patients with well-moderately differentiated SCCC and 12 patients with poorly differentiated SCCC. 20 healthy volunteers were enrolled as a control group. A bi-exponential model (BEM) analysis was performed to derive ADC, pure molecular diffusion coefficient (D), pseudo-diffusion coefficient (D^*) and perfusion fraction (f). The APT signal intensity (APT SI), ADC, D, D^* and f were measured. The parameters between the groups were compared with independent t-tests. Diagnostic performance was evaluated with a ROC analysis.

Results: The APT SI of SCCC (2.92 ± 0.24%) was higher than that of normal cervical stroma (2.72 ± 0.36%) with $P = 0.020$. The comparison of the AUCs for the diagnosis of SCCC was ADC > f > APT SI > D^* > D. A significant difference was found in the APT SI between the well-moderately differentiated SCCC group (2.82 ± 0.15%) and the poorly differentiated SCCC group (3.09 ± 0.27%) with $P = 0.006$. Except for D ($P = 0.012$), the ADC, D^* and f values were not significantly different between the groups ($P > 0.05$). The comparison of the AUCs for distinguishing poorly differentiated SCCC was APT SI > D > ADC > $D^* = f$.

Conclusion: APT imaging may be a useful technique in the diagnosis and predicting the differentiation of SCCC.

1. Introduction

Cervical cancer is one of the most common gynaecological tumors and is the leading cause of cancer mortality in women worldwide [1]. The prognostic factors include tumor volume, stage, pathological subtype and grade, and lymph node status [2]. Several novel methods for assessing the severity of uterine cervical cancer have been proposed, but histological assessment remains the basis for determining the treatment, clinical management and subsequent follow-up of patients [3]. Squamous cell carcinoma of the cervix (SCCC) is the most common pathological subtype of cervical cancer. An accurate preoperative evaluation of SCCC is crucial and challenging, as routine methods to assess the histological grading, preoperative biopsy and International Federation of Gynecology and Obstetrics (FIGO) clinical staging do not always accurately match the postoperative pathology [4–6].

Many investigators have attempted to develop imaging biomarkers for the grading of SCCC. MRI has superior soft tissue contrast that can clearly distinguish structures of the uterus. The bi-exponential model (BEM) intravoxel incoherent motion (IVIM) imaging not only considers true diffusion effects using a pure molecular diffusion coefficient (D) but also considers the influence of the microcirculation of blood in capillaries using perfusion-related parameters, including the pseudo-diffusion coefficient (D^*) and perfusion fraction (f). Several studies have concluded that BEM-derived metrics might be superior to the ADC in tumor diagnosis and pathological grade prediction [7–9]. Lin et al. [10] indicated that f and D may offer additional information in the diagnosis of cervical carcinoma, predicting pathological tumor subtypes and grades. However, the values of different pathological subtypes or grades obtained from these methods frequently have an overlapping range that may yield conflicting results [11]. Therefore,

* Corresponding author at: Department of Radiology, Shengjing Hospital of China Medical University, Sanhao Street No.36, Heping District, Shenyang, Liaoning, PR China.
E-mail address: sunhongzan@126.com (H. Sun).

https://doi.org/10.1016/j.mri.2019.08.020
Received 25 December 2018; Received in revised form 14 June 2019; Accepted 15 August 2019

Table 1
Details of MRI parameters.

Parameter	APT imaging	IVIM imaging	T1-weighted imaging	T2-weighted imaging
Imaging technique	3D Multishot TSE	MS Single-shot EPI	MS TSE	MS MultVane TSE
Repetition time/echo time (msec)	6294/5.9	3500/75	400/8	3000/100
Flip angle (degree)	90	90	90	90
Field of view (mm^2)	230 × 355	300 × 218	200 × 200	200 × 200
Matrix (frequency × phase)	116 × 177	100 × 72	268 × 200	200 × 200
Spatial resolution (mm^2)	2.0 × 2.0	3.0 × 3.0	0.75 × 1	1.0 × 1.0
Section thickness (mm)	5	4	4	4
Section gap (mm)	N/A	2	0.4	0.4
No. of sections	9	20	24	24
No. of signals acquired	2	2	1	1
ETL (TSE factor)	158	N/A	4	24
EPI factor	N/A	35	N/A	N/A
SENSE factor	3	3	4 (CS-SENSE)	2
mDIXON	no	no	yes	no
Fat suppression	SPIR	SPAIR	no	no
Total imaging time (min:*sec*)	05:46	04:44	01:17	01:18

ETL, echo train length; EPI, echo planar imaging; SENSE, sensitivity encoding; SPAIR, spectral attenuation with inversion recovery; 3D, three-dimensional; TSE, turbo spin echo; 2D, two-dimensional; N/A, not available.

Table 2
Intraclass correlation coefficients of the metrics for SCCC and normal cervical stroma.

	SCCC (95% CI)	Normal cervical stroma (95% CI)
APT SI (%)	0.68 (0.44, 0.83)	0.74 (0.46, 0.89)
ADC ($\times 10^{-3}$ mm^2/s)	0.89 (0.79, 0.95)	0.77 (0.51, 0.90)
D ($\times 10^{-3}$ mm^2/s)	N/A	0.47 (0.04, 0.75)
*D**($\times 10^{-3}$ mm^2/s)	0.36 (0.02, 0.63)	0.51 (0.10, 0.77)
f (%)	0.83 (0.68, 0.91)	0.80 (0.56, 0.91)

The data points are the intraclass correlation coefficients (ICCs). 95% CI, 95% confidence interval; N/A, not available; ADC, apparent diffusion coefficient; *D*, pure molecular diffusion; *D**, pseudo-diffusion coefficient; *f*, perfusion fraction.

developing a new MRI method is necessary to improve the accuracy of the grading of SCCC.

Amide proton transfer (APT) imaging has drawn considerable attention in the field of cellular and molecular imaging as a type of endogenous chemical exchange-dependent saturation transfer (CEST) imaging technique firstly developed by Zhou et al. [12], and recently got more mature with 3D image acquisition [13], that provides measurement of water signal intensity (SI) change through the exchange of protons between amide moieties and bulk water in a tissue. A frequency selective saturation pulse at 3.5 ppm relative to water proton frequency is used to saturate amide protons (-NH) in the peptide bonds of endogenous cytosolic proteins and peptides; then, the saturation is transferred to water protons through a proton exchange. The process is prolonged for a stronger change of bulk water signal [14]. Malignant gliomas are highly cellular tumors and have a higher cellular content of proteins and peptides than that of normal tissue, as revealed by MRI-guided proteomics [15] and in vivo MR spectroscopy [16]. Some previous experimental studies have also found a positive correlation between the APT signal and cellular proliferation [17]. Therefore, an increased APT signal has potential in indicating tumor cell proliferation and abnormal proteosynthesis. Based on published reports, APT imaging has been successfully applied to human brain tumors [18], thoracic lesions [19], prostate tumors [20], and head and neck tumor [21]. APT can be useful for predicting the histopathological grade of brain tumors [18,22,23], rectal cancer [24] and endometrial cancer [13].

However, there have not yet been any reports in testing feasibility of APT in the diagnosis and grading of SCCC comparing with IVIM-derived parameters. The purpose of this study was to prospectively assess the performance of APT imaging in diagnosing SCCC and predicting the level of differentiation of the SCCC tissues in a comparison of APT SI with IVIM-derived parameters (ADC, *D*, *D**, *f*).

2. Materials and methods

2.1. Study population

This prospective study was approved by the local institutional ethics committee, and written informed consent was obtained from all patients and healthy volunteers before performing MRI scans.

A total of 32 patients (median age 46 years; range 33–67 years) from February 2017 to July 2018 were enrolled in this study. None of the patients had received any prior treatments or had any contraindications for an MRI scan. MRI examinations were performed at least two weeks after a preoperative exfoliative endometrial cytologic evaluation in all the enrolled patients to avoid inaccurate measurements caused by local bleeding of cervical mucous membranes. The interval between the MRI scan and the surgery was < 2 weeks in all the patients. Firstly, 69 consecutive female patients with newly diagnosed SCCC proved by preliminary pathology were selected. Nineteen patients who did not have surgery to obtain pathology were excluded. Four of the patients were excluded because the postoperative pathology indicated an adenocarcinoma. Five patients were excluded because of an insignificant lesion dimension (the lesion area was < 30 mm^2). And Nine patients with severe artifacts, which could influence the measurement accuracy, were also excluded. Twenty of the 32 cases were well-moderately differentiated, and twelve cases were poorly differentiated.

Moreover, 20 healthy volunteers (median age 44 years; range 36–60 years), without any gynaecological disease, were recruited as a control group. The volunteers underwent an MRI scan, avoiding the menstrual period if they were not in menopause.

Table 3
Comparison between the metrics of SCCC and normal cervical stroma.

	SCCC (n = 32)	Normal cervical stroma (n = 20)	P	AUC	Optimal Cut-off value	Sensitivity (%)	Specificity (%)
APT SI (%)	2.92 ± 0.24	2.72 ± 0.36	0.020 (0.032,0.365)	0.696 (0.553, 0.816)	2.54	40.00	100.00
ADC ($\times 10^{-3}$ mm^2/s)	1.10 ± 0.27	1.56 ± 0.21	$P < 0.001$ (−0.610, −0.324)	0.902 (0.787, 0.967)	1.20	95.00	71.87
D ($\times 10^{-3}$ mm^2/s)	0.54 ± 0.13	0.59 ± 0.19	0.314 (−0.050,0.490)	0.586 (0.441, 0.721)	0.64	45.00	87.50
D^* ($\times 10^{-3}$ mm^2/s)	10.50 ± 3.10	8.80 ± 2.10	0.022 (0.258,3.158)	0.666 (0.521, 0.790)	9.12	75.00	59.38
f (%)	34.28 ± 11.48	52.50 ± 8.39	$P < 0.001$ (−23.771, −12.662)	0.889 (0.771, 0.959)	40.58	95.00	78.12

The data are the average ± standard deviation. Comparisons were performed by independent t-tests using SPSS. The AUC of the ROC curve for the metrics with the 95% confidence interval and the cut-off values were calculated using MedCalc. P values < 0.05 indicated significant differences.

2.2. MRI protocol

MRI was performed using a Philips 3.0T scanner (Ingenia CX, Philips Healthcare, Best, the Netherlands). Dual RF transmits were applied because of RF amplifier limitations. An optimized three-dimensional turbo spin echo sequence was integrated in APT protocol for better SNR and three-dimensional volume coverage. The saturation of the amide protons was maintained for about 2 s by continuous RF irradiation at the power of 2.0 μT, while each RF coil was turned on and off for 0.5 s [25]. The saturation RF pre-pulses were applied selectively at a frequency of ± 3.5 ppm from the water resonance to saturate the amide signal. And the resulting MTR (Magnetization Transfer Ratio) asymmetry is the Amide Proton Transfer weighted percentage. The accuracy of APT strongly depends on B0 homogeneity for calculating the Chemical Exchange Saturation Transfer(CEST) effect. Two more acquisitions at +3.5 ppm are performed with slightly different echo shifts on the order of 0.5 milliseconds, and the image volumes with 3 different echo times were used to calculate B0 field map. An APT z-spectrum was acquired with 4 more saturation frequency offsets (3.5 ± 0.8 ppm and − 3.5 ± 1.6 ppm); and the Z-spectrum is aligned per voxel to correct B0 field inhomogeneity. The dS Torso coil was used in addition to embedded coils to collect signa. The Z-spectrum signal correction and APT calculation were performed in-line after scan sections.

We acquired 11 b values (0, 10, 20, 50, 100, 200, 400, 800, 1200, 1600 and 2000 s/mm^2) in the axial plane covering 20 slices for IVIM imaging. ADC map was generated based on IVIM images, with b values of 0,100 and 800 s/mm^2. We added b = 100 s/mm^2 in diffusion measurement to reduce the capillary perfusion effect in a small b value range in ADC quantification. D, D^*, f were generated based on the nonlinear bi-exponential model according to the following formula: $S(b)/S_0 = (1\text{-}f)\exp.(-b \times D) + f \exp.(-b \times D^*)$, where $S(b)$ represents the mean signal intensity with diffusion gradient b, S_0 represents the mean signal intensity when b = 0 s/mm^2, D represents the pure molecular diffusion coefficient, D^* represents the pseudo-diffusion coefficient, f is the microvascular volume fraction. More details for MR imaging are summarized in Table 1.

2.3. Image and data analysis

The data set was evaluated using Philips postprocessing workstation. The acquired APT raw data were imported into the IDL application (Research Systems, Boulder, Colorado) for analysis. The Script software (IVIM version 3.2), written in MATLAB 2014, was used for the IVIM data analysis. Two observers with 21 years (W.H.W.) and 13 years (S.Y.) of experience in MRI measured the resulting parameters in a manner that was blinded to patient information individually. For the patient groups, the slice with the maximum cross-sectional tumor area on the axial T2WI MRI image was selected. An ROI containing the entire tumor region was manually delineated using a freehand tool, and the ROI was then copied to the corresponding APT image to obtain the APT SI. Then the ROI was drawn on the corresponding slice on the IVIM imaging. Postprocessing software automatically copied the ROI to other b-value images to obtain the D, D^*, and f. Every ROI was carefully positioned to avoid necrosis, haemorrhage, calcification, and artifacts. For the healthy group, ROIs were drawn to identify all the cervical stroma excluding the mucosa. The averaged values of the two observers were recorded for further analysis. The postoperative specimens, which were prepared and analysed by the pathology department of our hospital. The more predominant differentiation was selected when different levels of differentiation coexisted within the same tumor.

2.4. Statistical analysis

Statistical analysis was accomplished with the MedCalc 15.2.0 and SPSS 20.0 software (IBM SPSS Statistics, version 20.0; IBM Japan, Tokyo, Japan). $P < 0.05$ was considered statistically significant. The

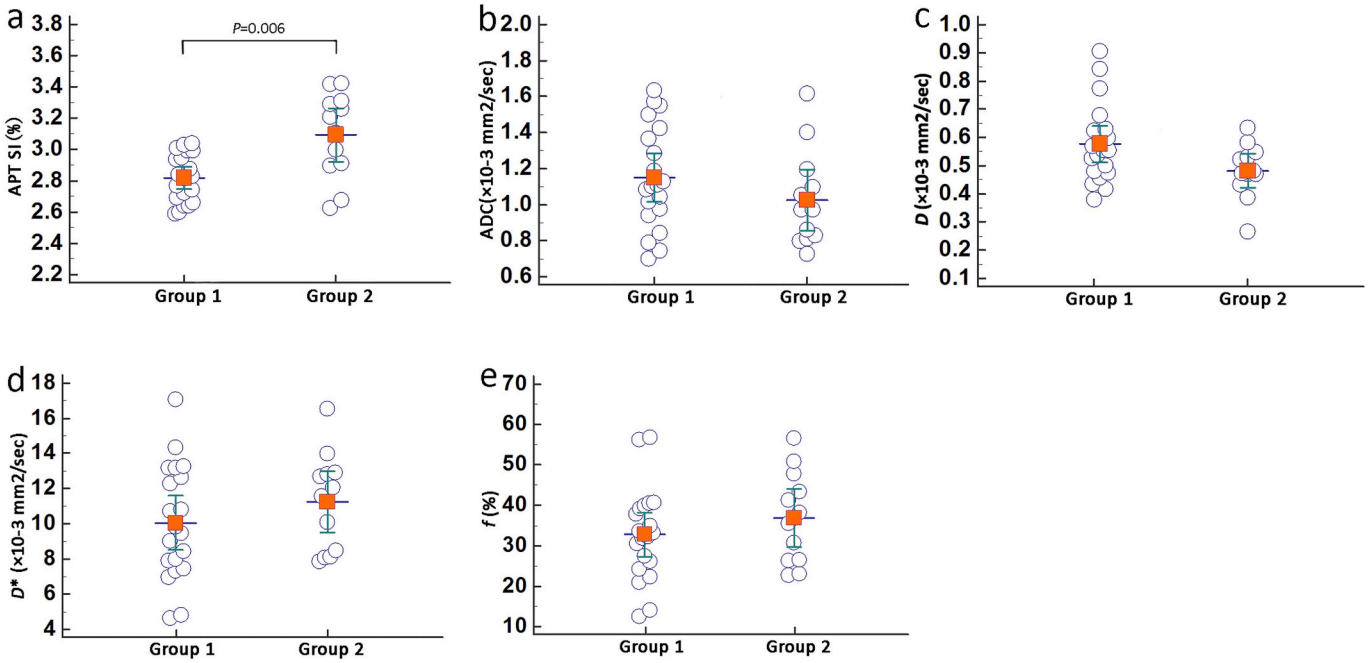

Fig. 1. Plots of the parameters in well-moderately differentiated SCCC and poorly differentiated SCCC (a)–(e): circles are individual data points of the average values from two readers. Transverse lines and vertical lines are averages and standard deviations, respectively. Well-moderately differentiated SCCC and poorly differentiated SCCC groups are marked as group 1 and group 2, respectively. Details of the average and standard deviation values for each parameter are shown in Table 4.

Shapiro-Wilk test was used to test for the normality of the metrics. A two-way model average measure intraclass correlation coefficient (ICC) was used to test the interobserver agreement based on the following criteria: < 0.40, poor agreement; 0.40–0.59, fair agreement; 0.60–0.74, good agreement; and ≥0.75, excellent agreement. The metrics of the normal cervical stroma and SCCC and the metrics of SCCC with different levels of histological differentiation were compared using independent *t*-tests for the normally distributed data or the Kruskal-Wallis H test for the data with a non-normal distribution. A receiver operating characteristic(ROC) analysis was conducted to investigate the diagnostic performance of the parameters.

3. Results

3.1. Shapiro-Wilk test and interobserver agreement

The Shapiro-Wilk test showed the *D* value of observer 1($P = 0.04$) and observer 2 ($P = 0.001$) were not normally distributed, while the other metrics of the two observers were normally distributed ($P > 0.05$). The averaged values of the metrics getting form two observers were calculated and analysed as well: SCCC group: APT SI, $P = 0.07$; ADC, $P = 0.10$; *D*, $P = 0.07$; *D**, $P = 0.44$; *f*, $P = 0.50$, normal cervical stroma group: APT SI, $P = 0.28$; ADC, $P = 0.52$; *D*, $P = 0.61$; *D**, $P = 0.06$; *f*, $P = 0.32$.

A good agreement was obtained between the APT SI values from the two observers with a moderate ICC value (0.68 for the SCCC group and 0.74 for the normal cervical stroma group). The ICCs of ADC (0.89) and *f* (0.83) of the SCCC tissues and the ICC of ADC (0.77) and *f* (0.80) of the normal cervical stroma were higher than that of the APT SI. Meanwhile, a poor agreement was found between the *D** of the SCCC tissues from two observers (ICC = 0.36), as shown in Table 2. The ICC of *D* in the SCCC group could not be obtained for non-normal distribution.

3.2. Comparison between the metrics of SCCC and normal cervical stroma

The independent *t*-tests showed the APT SI, ADC, *D** and *f* showed significant differences between the SCCC group and the control group, while there were no significant differences in the *D* value between these two groups (Table 3). The APT SI of SCCC was higher than that of normal cervical stroma ($P = 0.020$).

The AUC of the APT SI had significant differences compared to those of the ADC ($P = 0.039$, 95% CI: 0.011, 0.400) and *f* ($P = 0.024$; 95% CI: 0.025, 0.361), as shown in Fig. 2. The comparison of the AUCs was ADC > *f* > APT SI > *D** > *D*.

3.3. Comparison of the metrics between well-moderately differentiated SCCC and poorly differentiated SCCC

The distributions of the APT SI, ADC, *D*, *D** and *f* in SCCC are shown in Fig. 1. A statistical difference in the APT SI ($P = 0.006$) and *D* ($P = 0.012$) between the well-moderately differentiated SCCC and poorly differentiated SCCC was observed, while there were no significant differences in the ADC, *D** or *f* values of these two groups (Table 4). Poorly differentiated SCCC tissues had higher APT values than did well-moderately differentiated SCCC (Figs. 2 and 3).

The AUC of the APT SI was higher than the AUCs of the ADC, *D*, *D** and *f* (Fig. 2). Significant differences were found between the AUC of the APT SI and that of the *f* ($P = 0.018$, 95% CI: 0.031, 0.335). The comparison of the AUCs was APT SI > *D* > ADC > *D** = *f*. The typical cases are shown in Figs. 3–5.

Table 4
Comparison of the metrics between well-moderately differentiated SCCC and poorly differentiated SCCC.

	Well-moderately differentiated (n = 20)	Poorly differentiated (n = 12)	P (95% CI)	AUC (95% CI)	Optimal cut-off value	Sensitivity (%)	Specificity (%)
APT SI (%)	2.82 ± 0.15	3.09 ± 0.27	0.006 (−0.428, −0.122)	0.792 (0.612, 0.914)	3.04	58.33	100.00
ADC ($\times 10^{-3}$ mm^2/s)	1.14 ± 0.27	1.03 ± 0.27	0.260 (−0.088, 0.313)	0.633 (0.445, 0.796)	0.97	58.33	75.00
D ($\times 10^{-3}$ mm^2/s)	0.58 ± 0.14	0.47 ± 0.10	0.016(0.023,0.208)	0.754 (0.570, 0.889)	0.53	83.33	65.00
D^* ($\times 10^{-3}$ mm^2/s)	10.01 ± 3.27	11.25 ± 2.75	0.297 (−3.501,1.108)	0.608 (0.421, 0.775)	8.00	91.67	35.00
f (%)	32.72 ± 11.56	36.88 ± 11.35	0.329 (−12.725, 4.405)	0.608 (0.421, 0.775)	40.583	41.67	90.00

The data are the average ± standard deviation. Comparisons were performed by independent t-tests using SPSS. The AUC of the ROC curve for the metrics with the 95% confidence interval and the cut-off values were calculated using MedCalc. P values < 0.05 indicated significant differences.

4. Discussion and conclusions

Good agreement was obtained with APT imaging in the present study with a moderate ICC value. And the APT SI in the SCCC group was higher than that in the normal cervical stroma group. Additionally, the APT SIs of poorly differentiated SCCCs was lower than that of well-moderately differentiated SCCCs. APT may show a better performance than IVIM-derived parameters (ADC, D, D^*, and f) in predicting SCCC differentiation.

As in previous studies, good repeatability in the measurement of APT has been reported in adult gliomas [22,26]. A recent study in endometrial adenocarcinoma also revealed excellent interobserver agreement with APT SI (ICC, 0.92; 95% CI: 0.85, 0.96), which was better than that of the mean ADC (ICC, 0.84; 95% CI: 0.68, 0.92) and the minimum ADC(ICC, 0.74; 95% CI: 0.46, 0.87) [13]. Compared to the results above, APT interobserver agreement in the present study was slightly lower. This result may be related to the unsatisfactory APT imaging resolution caused by severe motion artifacts, which may lead to difficult identification of the lesions. And some lesions included in our study were relatively small which may affect the accurate positioning of ROIs. In addition, not only the APT SI but also the IVIM-derived parameters had substantial overlaps in measurements, which may limit their application in clinical practice.

APT technology has been successfully applied in endometrioid endometrial adenocarcinoma (EEA) [13]. The study of Takayama et al. found that the APT SI was positively correlated with the histologic grades of EEA. The aggressive EEAs showed high APT SIs, but less-aggressive EEAs showed low APT SIs (Grade 1: 2.2 ± 0.2%, Grade 2: 3.2 ± 0.3%, Grade 3: 3.7 ± 0.3%). Our study yielded similar results: the poorly differentiated SCCCs has lower APT SIs than that of well-moderately differentiated SCCCs. APT imaging has been used to visualize endogenous mobile proteins and peptides [27,28]. There have been several studies demonstrating the relationship between the APT signal and protein expression [22,25]. The heterogeneity of APT images may be manifested by different components within the tumors. The high signal intensity of APT may represent the active metabolism of tumors and the production of large amounts of proteins. Tumor angiogenesis may also be another reason for the increase of APT, which includes the division rate of vascular cells or the spatial density of capillaries. Where APT signal is relatively low, it may be the fibrous components of tumors. Similarly, the areas with abundant tumor cells in the lesions tend to have more cells, denser intensity, which limits the diffusion. And the angiogenesis increase blood volume in the tissue. While the areas with fewer tumor cells, such as the central area, have decreased blood supply, increased necrotic tissue, resulting in heterogeneous changes in IVIM images. Compared to the ADC and f, the APT SI had a smaller AUC and relatively low sensitivity, but a better specificity. From this perspective, the changes in the diffusion of water molecules and perfusion into the extracellular space may be more sensitive to detect than changes in intracellular mobile proteins and peptides in SCCC tissues. However, the source of the APT signal is not clear yet. The APT effect has been correlated with the T1 of water, the background magnetization transfer effect, the nuclear Overhauser effects of aliphatic protons, and the water content of tissues [29,30]. Overall, further investigation is needed to determine the mechanisms of APT contrast in tumors.

To the best of our knowledge, this investigation is the first study to explore APT imaging in SCCC and to compare the APT SI with IVIM-derived parameters. Previous studies only compared APT with DWI-generated ADC values. Takayama et al. suggested that the diagnostic performance of APT is superior to that of the mean and minimum ADCs in endometrial cancer grading [13]. Regarding cervical cancer, negative correlations [31] or weak correlations [32] have been found between the ADC and pathological grade, which supports the findings of this present study. Nevertheless, the ability of BEM-derived parameters to distinguish well-moderately differentiated SCCC and poorly

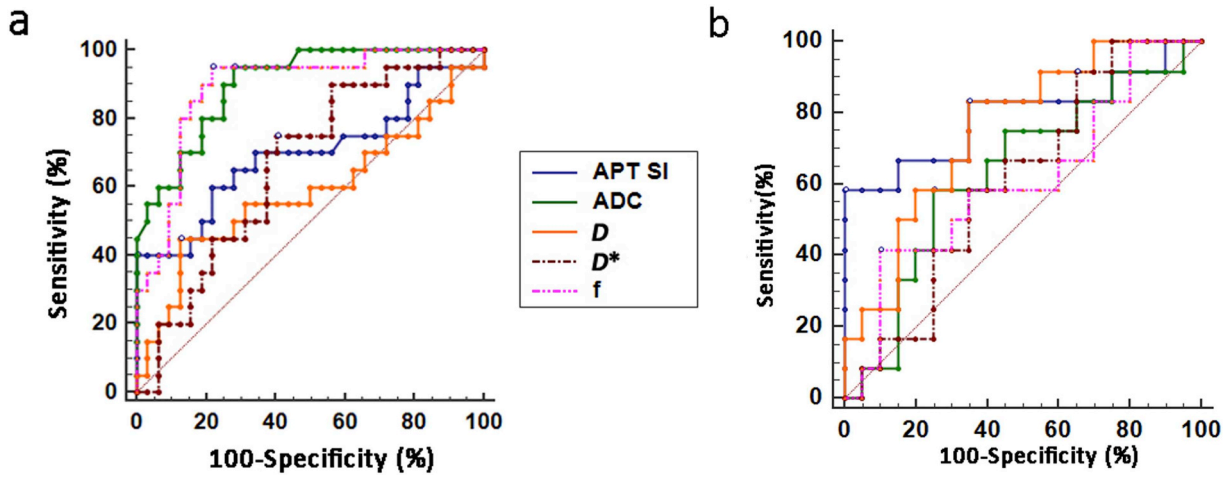

Fig. 2. ROC analysis of the APT SI, ADC, *D*, *D**, and *f*. (a) Differentiation of SCCC from normal cervical stroma. The comparison of the AUCs: ADC > *f* > APT SI > *D** > *D*. (b) Differentiation of poorly differentiated SCCC from well-moderately differentiated SCCC. The comparison of the AUCs: APT SI > *D* > ADC > *D** = *f*.

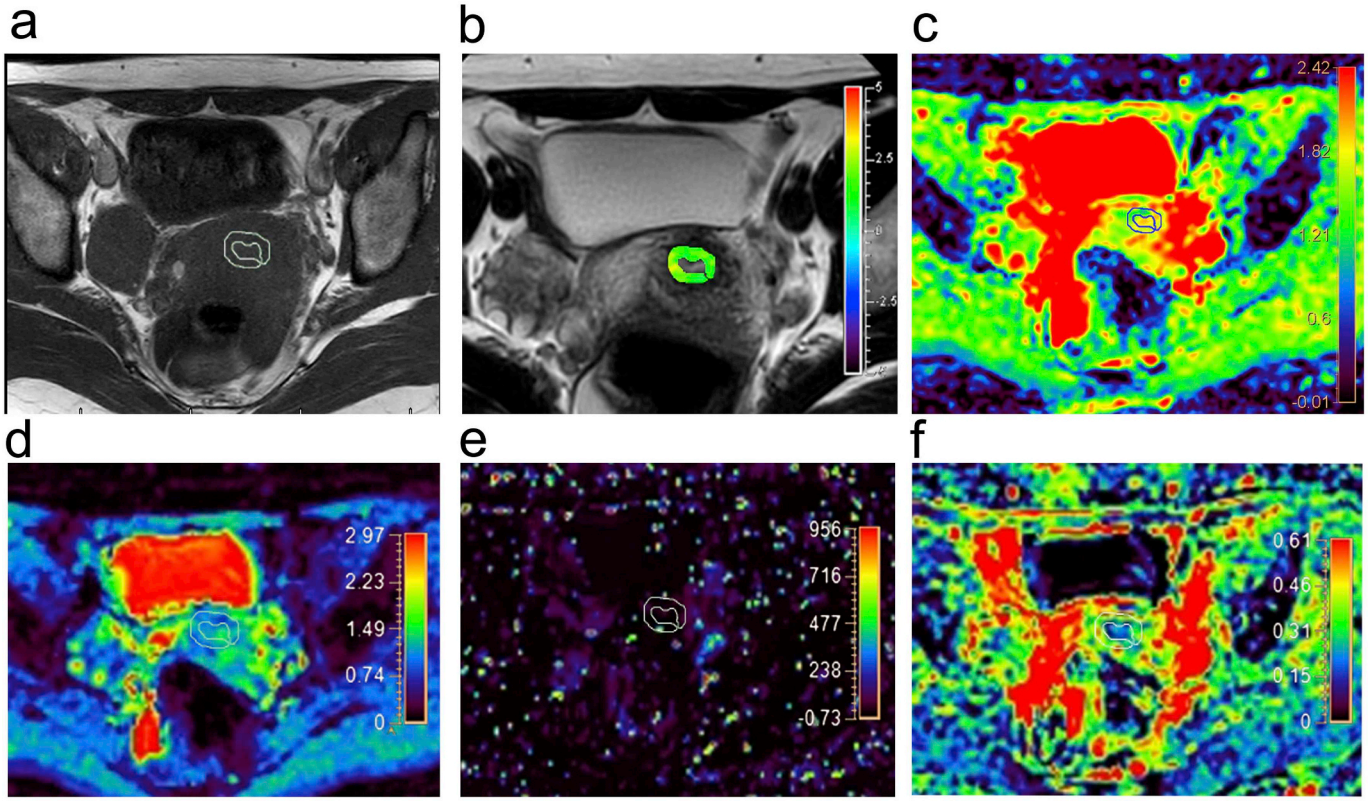

Fig. 3. Normal cervix of a 45-year-old healthy female volunteer. (a) Axial T1-weighted image (b) Axial T2-weighted image with APT imaging shows cervical stroma with a low signal intensity of 2.69%. (c–f) ADC map generated from IVIM imaging with b values of 0, 100 and 800 s/mm^2 shows cervical stroma with a value of 1.63×10^{-3} mm^2/s, The *D*, *D**, and *f* maps from a BEM of the IVIM data shows that these values for the normal cervix were 0.67×10^{-3} mm^2/s, 8.56×10^{-3} mm^2/s and 56.39%, respectively.

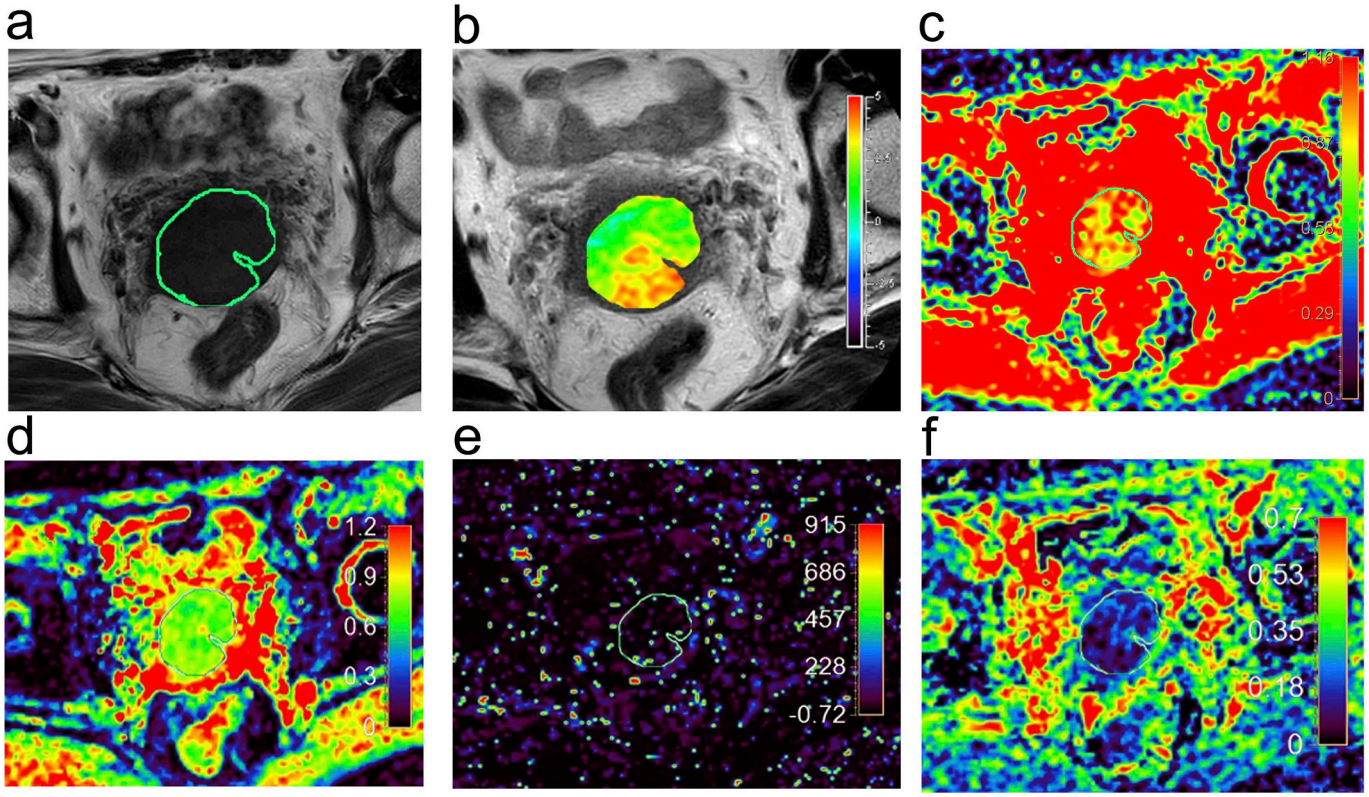

Fig. 4. A 39-year-old woman with well-moderately differentiated SCCC. (a) Axial T1-weighted image (b) Axial T2-weighted image with APT imaging shows an irregular mass with a relatively high signal intensity of 2.74%. (c–f) ADC map generated from IVIM imaging with b values of 0, 100 and 800 s/mm^2 shows cervical stroma with a value of 0.75×10^{-3} mm^2/s, The D, D^*, and f maps from a BEM of the IVIM data shows that these values for the normal cervix were 0.46×10^{-3} mm^2/s, 4.82×10^{-3} mm^2/s and 24.14%, respectively.

differentiated SCCC is still unclear. Dynamic contrast-enhanced MR imaging (DCE-MRI) describes changes in signal intensity over time reflecting the microcirculation of tumors [33]. In a previous study, DCE-MRI performs well for tumor detection in cervical cancer, with a total diagnostic accuracy was 0.96 for differentiation of malignant lesions and benign lesions [34]. But another study shows it does not improve staging accuracy compared to T2WI alone [35]. Compared with DCE-MRI, APT and IVIM do not require injections of contrast agents and can reflect the intrinsic changes of tumors at the molecular level.

Several limitations of this study must be considered. First, the patient population was not large enough, and other pathological subtypes of cervical carcinoma, such as adenocarcinoma and small cell carcinoma, were not included in this study, which might cause statistical deviations. Second, we selected the maximum cross-sectional tumor area to draw the ROIs without covering the whole tumor. However, a previous study has shown that there is little effect for different measurements on APT imaging in glioma grading [36]. Furthermore, an imperfect APT imaging quality made the ROI selection less consistent for the observers. We abandoned the cases with severe artifacts and small lesions, which may have artificially overestimated the value of APT imaging. To improve the accuracy of APT assessment in tumors, new observers need more practice in evaluating the APT image quality and drawing an appropriate ROI that avoids necrosis, haemorrhage, calcification, and especially artifacts. In the future, large-scale investigations should be performed to confirm the value of APT imaging in SCCC diagnosis and differentiation. We should also conduct further studies to explore the potential associations between APT imaging and the molecular components of SCCC.

In conclusion, APT imaging may be a useful technique for providing helpful information to assist in the diagnosis and differentiation of SCCC, with a diagnostic accuracy comparable to that of the parameters derived from IVIM.

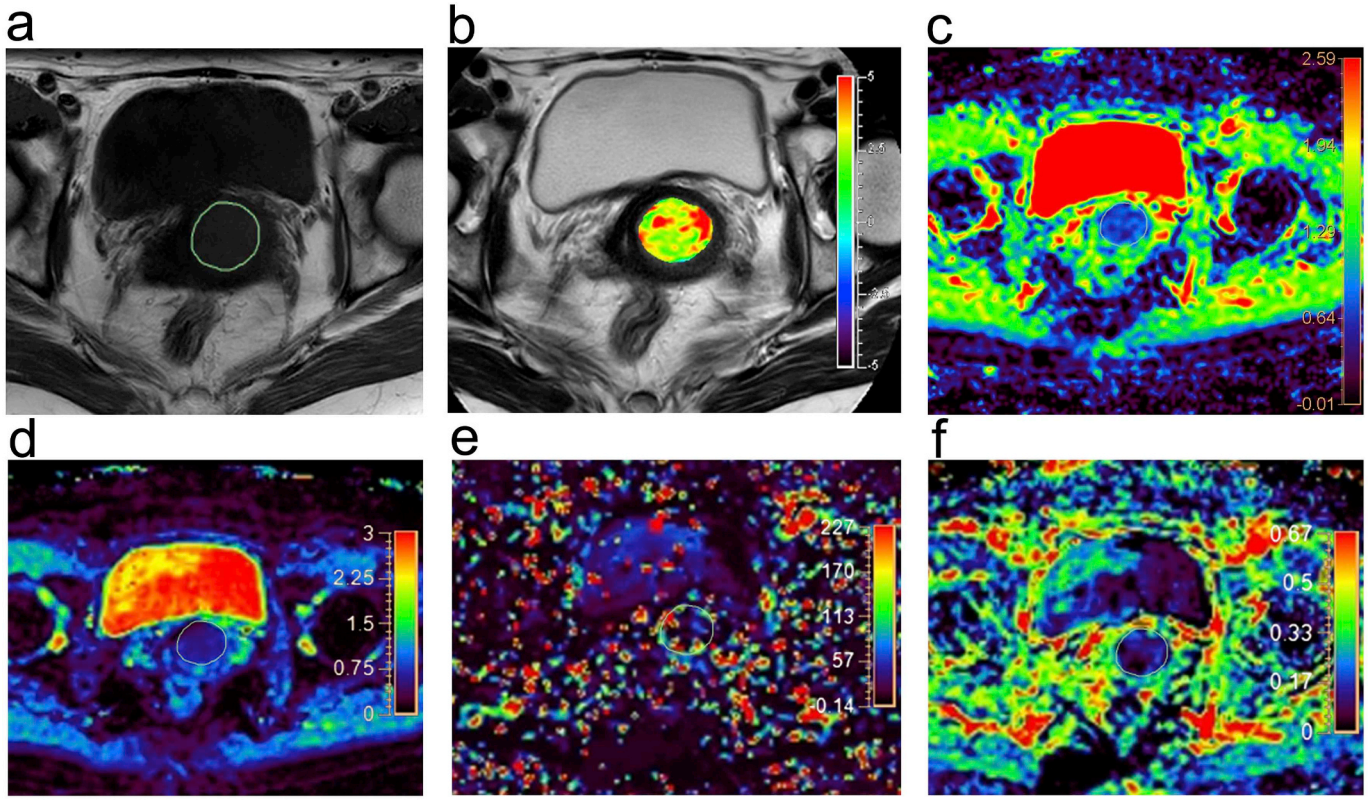

Fig. 5. A 55-year-old woman with poorly differentiated SCCC. (a) Axial T1-weighted image (b) Axial T2-weighted image with APT imaging shows an irregular mass with a high signal intensity of 2.91%. (c–f) ADC map generated from IVIM imaging with b values of 0, 100 and 800 s/mm^2 shows cervical stroma with a value of 0.73×10^{-3} mm^2/s, The *D*, *D**, and *f* maps from a BEM of the IVIM data shows that these values for the normal cervix were 0.42×10^{-3} mm^2/s, 8.07×10^{-3} mm^2/s and 30.68%, respectively.

Acknowledgments

The authors gratefully acknowledge the assistance of Baohai Sun, Jinsong Liu and Guoqing Wang for assisting in patient scans.

References

[1] Sala E, Rockall AG, Freeman SJ, Mitchell DG, Reinhold C. The added role of MR imaging in treatment stratification of patients with gynecologic malignancies: what the radiologist needs to know. Radiology 2013;266(3):717–40.
[2] Liu Y, Bai R, Sun H, Liu H, Wang D. Diffusion-weighted magnetic resonance imaging of uterine cervical cancer. J Comput Assist Tomogr 2009;33(6):858–62.
[3] Robertson AJ, Anderson JM, Beck JS, Burnett RA, Howatson SR, Lee FD, et al. Observer variability in histopathological reporting of cervical biopsy specimens. J Clin Pathol 1989;42(3):231–8.
[4] Qin Y, Peng Z, Lou J, Liu H, Deng F, Zheng Y. Discrepancies between clinical staging and pathological findings of operable cervical carcinoma with stage IB-IIB: a retrospective analysis of 818 patients. Aust N Z J Obstet Gynaecol 2009;49(5):542–4.
[5] Choi HJ, Ju W, Myung SK, Kim Y. Diagnostic performance of computer tomography, magnetic resonance imaging, and positron emission tomography or positron emission tomography/computer tomography for detection of metastatic lymph nodes in patients with cervical cancer: meta-analysis. Cancer Sci 2010;101(6):1471–9.
[6] Chung HH, Kang SB, Cho JY, Kim JW, Park NH, Song YS, et al. Can preoperative MRI accurately evaluate nodal and parametrial invasion in early stage cervical cancer? Jpn J Clin Oncol 2007;37(5):370–5.
[7] Woo S, Lee JM, Yoon JH, Joo I, Han JK, Choi BI. Intravoxel incoherent motion diffusion-weighted MR imaging of hepatocellular carcinoma: correlation with enhancement degree and histologic grade. Radiology 2014;270(3):758–67.
[8] Chandarana H, Lee VS, Hecht E, Taouli B, Sigmund EE. Comparison of biexponential and monoexponential model of diffusion weighted imaging in evaluation of renal lesions: preliminary experience. Invest Radiol 2011;46(5):285–91.
[9] Liu C, Liang C, Liu Z, Zhang S, Huang B. Intravoxel incoherent motion (IVIM) in evaluation of breast lesions: comparison with conventional DWI. Eur J Radiol 2013;82(12):e782–9.
[10] Lin M, Yu X, Chen Y, Ouyang H, Wu B, Zheng D, et al. Contribution of mono-exponential, bi-exponential and stretched exponential model-based diffusion-weighted MR imaging in the diagnosis and differentiation of uterine cervical carcinoma. Eur Radiol 2017;27(6):2400–10.
[11] Lam WW, Poon WS, Metreweli C. Diffusion MR imaging in glioma: does it have any role in the pre-operation determination of grading of glioma? Clin Radiol 2002;57(3):219–25.
[12] Zhou J, Payen JF, Wilson DA, Traystman RJ, van Zijl PC. Using the amide proton signals of intracellular proteins and peptides to detect pH effects in MRI. Nat Med 2003;9(8):1085–90.
[13] Takayama Y, Nishie A, Togao O, Asayama Y, Ishigami K, Ushijima Y, et al. Amide proton transfer MR imaging of endometrioid endometrial adenocarcinoma: association with histologic grade. Radiology 2018;286(3):909–17.
[14] Kogan F, Hariharan H, Reddy R. Chemical exchange saturation transfer (CEST) imaging: description of technique and potential clinical applications. Curr Radiol Rep 2013;1(2):102–14.
[15] Hobbs SK, Shi G, Homer R, Harsh G, Atlas SW, Bednarski MD. Magnetic resonance image-guided proteomics of human glioblastoma multiforme. J Magn Reson Imaging 2003;18(5):530–6.
[16] Howe FA, Barton SJ, Cudlip SA, Stubbs M, Saunders DE, Murphy M, et al. Metabolic profiles of human brain tumors using quantitative in vivo 1H magnetic resonance spectroscopy. Magn Reson Med 2003;49(2):223–32.
[17] Sagiyama K, Mashimo T, Togao O, Vemireddy V, Hatanpaa KJ, Maher EA, et al. In vivo chemical exchange saturation transfer imaging allows early detection of a therapeutic response in glioblastoma. Proc Natl Acad Sci U S A 2014;111(12):4542–7.
[18] Bai Y, Lin Y, Zhang W, Kong L, Wang L, Zuo P, et al. Noninvasive amide proton transfer magnetic resonance imaging in evaluating the grading and cellularity of gliomas. Oncotarget 2017;8(4):5834–42.
[19] Ohno Y, Yui M, Koyama H, Yoshikawa T, Seki S, Ueno Y, et al. Chemical exchange saturation transfer MR imaging: preliminary results for differentiation of malignant and benign thoracic lesions. Radiology 2016;279(2):578–89.
[20] Takayama Y, Nishie A, Sugimoto M, Togao O, Asayama Y, Ishigami K, et al. Amide proton transfer (APT) magnetic resonance imaging of prostate cancer: comparison with Gleason scores. Magma (New York, NY) 2016;29(4):671–9.
[21] Law BKH, King AD, Ai QY, Poon DMC, Chen W, Bhatia KS, et al. Head and neck tumors: amide proton transfer MRI. Radiology 2018;288(3):782–90.
[22] Togao O, Yoshiura T, Keupp J, Hiwatashi A, Yamashita K, Kikuchi K, et al. Amide proton transfer imaging of adult diffuse gliomas: correlation with histopathological grades. Neuro-oncology 2014;16(3):441–8.
[23] Togao O, Hiwatashi A, Yamashita K, Kikuchi K, Keupp J, Yoshimoto K, et al. Grading diffuse gliomas without intense contrast enhancement by amide proton transfer MR imaging: comparisons with diffusion- and perfusion-weighted imaging. Eur Radiol 2017;27(2):578–88.
[24] Nishie A, Takayama Y, Asayama Y, Ishigami K, Ushijima Y, Okamoto D, et al. Amide proton transfer imaging can predict tumor grade in rectal cancer. Magn Reson

Imaging 2018;51:96–103.
[25] Zhou J, Zhu H, Lim M, Blair L, Quinones-Hinojosa A, Messina SA, et al. Three-dimensional amide proton transfer MR imaging of gliomas: initial experience and comparison with gadolinium enhancement. J Magn Reson Imaging 2013;38(5):1119–28.
[26] Sakata A, Okada T, Yamamoto Y, Fushimi Y, Dodo T, Arakawa Y, et al. Addition of amide proton transfer imaging to FDG-PET/CT improves diagnostic accuracy in glioma grading: a preliminary study using the continuous net reclassification analysis. AJNR Am J Neuroradiol 2018;39(2):265–72.
[27] Zhou J, Lal B, Wilson DA, Laterra J, van Zijl PC. Amide proton transfer (APT) contrast for imaging of brain tumors. Magn Reson Med 2003;50(6):1120–6.
[28] Wen Z, Hu S, Huang F, Wang X, Guo L, Quan X, et al. MR imaging of high-grade brain tumors using endogenous protein and peptide-based contrast. NeuroImage 2010;51(2):616–22.
[29] Scheidegger R, Wong ET, Alsop DC. Contributors to contrast between glioma and brain tissue in chemical exchange saturation transfer sensitive imaging at 3 Tesla. NeuroImage 2014;99:256–68.
[30] Xu J, Zaiss M, Zu Z, Li H, Xie J, Gochberg DF, et al. On the origins of chemical exchange saturation transfer (CEST) contrast in tumors at 9.4 T. NMR Biomed 2014;27(4):406–16.
[31] Payne GS, Schmidt M, Morgan VA, Giles S, Bridges J, Ind T, et al. Evaluation of magnetic resonance diffusion and spectroscopy measurements as predictive biomarkers in stage 1 cervical cancer. Gynecol Oncol 2010;116(2):246–52.
[32] Liu Y, Ye Z, Sun H, Bai R. Clinical application of diffusion-weighted magnetic resonance imaging in uterine cervical cancer. Int. J. Gynecol. Cancer 2015;25(6):1073–8.
[33] Brix G, Semmler W, Port R, Schad LR, Layer G, Lorenz WJ. Pharmacokinetic parameters in CNS Gd-DTPA enhanced MR imaging. J Comput Assist Tomogr 1991;15(4):621–8.
[34] Kuang F, Yan Z, Li H, Feng H. Diagnostic accuracy of diffusion-weighted MRI for differentiation of cervical cancer and benign cervical lesions at 3.0T: comparison with routine MRI and dynamic contrast-enhanced MRI. J Magn Reson Imaging 2015;42(4):1094–9.
[35] Van Vierzen PB, Massuger LF, Ruys SH, Barentsz JO. Fast dynamic contrast enhanced MR imaging of cervical carcinoma. Clin Radiol 1998;53(3):183–92.
[36] Sakata A, Okada T, Yamamoto A, Kanagaki M, Fushimi Y, Okada T, et al. Grading glial tumors with amide proton transfer MR imaging: different analytical approaches. J Neurooncol 2015;122(2):339–48.